

Silica Restricting the Sulfur Volatilization of Nickel Sulfide for High-Performance Lithium-Ion Batteries

Qidong Li, Li Li, Peijie Wu, Nuo Xu, Liang Wang, Matthew Li, Alvin Dai, Khalil Amine, Liqiang Mai,* and Jun Lu*

Nickel sulfides are regarded as promising anode materials for advanced rechargeable lithium-ion batteries due to their high theoretical capacity. However, capacity fade arising from significant volume changes during operation greatly limits their practical applications. Herein, confined NiS_x@C yolk-shell microboxes are constructed to address volume changes and confine the active material in the internal void space. Having benefited from the yolk-shell structure design, the prepared NiS_x@C yolk-shell microboxes display excellent electrochemical performance in lithium-ion batteries. Particularly, it delivers impressive cycle stability (460 mAh g⁻¹ after 2000 cycles at 1 A g⁻¹) and superior rate performance (225 mAh g⁻¹ at 20 A g⁻¹). Furthermore, the lithium storage mechanism is ascertained with in situ synchrotron high-energy X-ray diffractions and in situ electrochemical impedance spectra. This unique confined yolk-shell structure may open up new strategies to create other advanced electrode materials for high performance electrochemical storage systems.

As an important component within energy storage systems, rechargeable batteries, especially rechargeable lithium-ion batteries, have been extensively studied since the 1960s and 1970s and are now widely used in portable devices, electric vehicles, and even in grid-connected power generation systems. With the rapid development of society, energy storage systems of increasing performance parameters are desired, accelerating the research of high-performance rechargeable lithium-ion batteries tremendously.^[1–3] For practical applications, both resource availability and electrochemical performance of electrode materials

are important factors. More efforts are required to develop low-cost and efficient electrode materials.^[4,5] As an important part of battery components, anode materials have been one of the most critical and extensively studied aspects in electrochemical research.^[6–10] Among the many anode materials, transition metal-based compounds are characterized as a promising species due to their abundant reserves and multiple valence nature. Having more electrons involved in electrochemical reactions can provide higher capacity that meet the energy density requirements of modern electrochemical storage devices.^[11,12] In this regard, many efforts have been made to discover new transition metal-based anode materials such as carbides, oxides, phosphides, or sulfides.^[13–15]

Due to its abundance and low prices, mineral-type nickel sulfide has gained much attention in photo-electrochemistry and is widely used in semiconductor, magnetic, photo-electrocatalytic, thermoelectric, phase-converting materials, and electrode materials for rechargeable lithium-ion batteries.^[16–20] In prior research, the numerous nickel sulfides applied in rechargeable lithium-ion batteries (NiS, NiS₂, Ni₃S₂, and Ni₃S₄) have all possessed high theoretical capacities (NiS/589, NiS₂/870, Ni₃S₂/445, and Ni₃S₄/703 mAh g⁻¹).^[20] However, nickel sulfides are seldom regarded as excellent candidates for lithium-ion batteries, mainly due to the instability in the nickel-rich active material. As a result, during lithiation and delithiation the active materials tend to be more susceptible to pulverization and collapse, making it difficult to form a stable interface. The everexpanding interface area between active materials and electrolyte will continuously consume Li⁺ to form the solid electrolyte interface (SEI), resulting in low coulombic efficiency. Meanwhile, the electrically insulated SEI layer will wrap the active materials to form “inactive island” which results in rapid capacity decay and poor cycle performance.^[21,22] Numerous strategies have been developed to address this issue, such as controlling cutoff voltage,^[20] constructing nanomaterials,^[21] and compositing with graphene.^[23,24] However, despite extensive research efforts, improving the performance of nickel sulfide to achieve high specific capacity and long cycle life is still a challenge.^[21,25,26]

Herein, a step-divided construction method was developed successfully to synthesize the NiS_x@carbon (NiS_x@C) yolk-shell microboxes via a template-assisted coating, thermal

Q. D. Li, L. Li, P. J. Wu, N. Xu, Prof. L. Q. Mai
State Key Laboratory of Advanced Technology for
Materials Synthesis and Processing
Wuhan University of Technology
Wuhan 430070, Hubei, China
E-mail: mlq518@whut.edu.cn

Q. D. Li, M. Li, A. Dai, Dr. K. Amine, Dr. J. Lu
Chemical Sciences and Engineering Division
Argonne National Laboratory
9700 South Cass Avenue, Lemont, IL 60439, USA
E-mail: junlu@anl.gov

L. Wang
Department of Physics
Northern Illinois University
DeKalb, IL 60115, USA

 The ORCID identification number(s) for the author(s) of this article can be found under <https://doi.org/10.1002/aenm.201901153>.

DOI: 10.1002/aenm.201901153

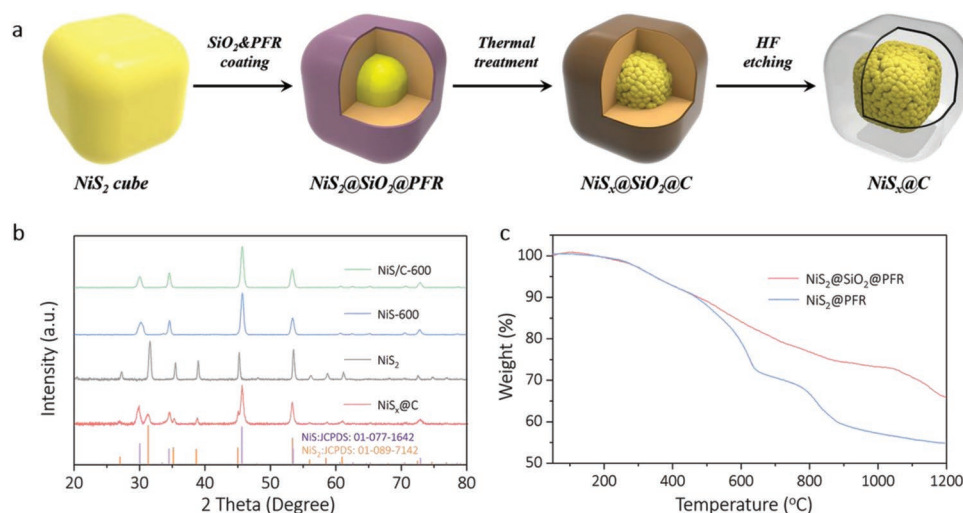


Figure 1. a) The schematic illustration of the synthesis procedure of $NiS_x@C$. b) XRD patterns of $NiS/C-600$, $NiS-600$, NiS_2 , and $NiS_x@C$. c) TGA curves of $NiS_2@SiO_2@PFR$ and $NiS_2@PFR$.

treatment, and etching process. By remaining in this confined structure, $NiS_x@C$ yolk–shell microboxes could not only produce a stable electrochemical reaction environment to buffer the severe volume expansion of NiS_x yolk during lithiation and delithiation but also help to form a stable SEI layer. Accordingly, the $Li/NiS_x@C$ battery is able to realize high capacity and stable cycling performance with $\approx 460 \text{ mAh g}^{-1}$ over 2000 cycles at a current density of 1 A g^{-1} and high reversible capacity to 790 mAh g^{-1} at 100 mA g^{-1} . In situ synchrotron high-energy X-ray diffractions (HEXRD) confirmed the nature of the conversion reaction while the kinetics of the $NiS_x@C$ electrode was also investigated via in situ electrochemical impedance spectra (EIS), which reveals an ultrastable $NiS_x@C$ electrode structure during the discharge/charge process. These improvements and mechanism analysis presented here serve as a solid foundation for the further study on conversion type anodes for energy storage systems.

The synthetic procedure for $NiS_x@C$ yolk–shell microboxes with a step-divided construction method is illustrated in Figure 1a. First, the precursor uniform NiS_2 cubes, synthesized through a facile solvothermal method, act as the precursor and coating template. Second, a layer composed of ultrafine silica nanoparticles is coated on the surface of the NiS_2 cubes, serving as a sacrificial template for creating buffer space, followed with a polymer coating of phenol formaldehyde resin (PFR) via condensation reaction. Third, $NiS_x@SiO_2@C$ microcubes are obtained after a carbonization treatment at 600 °C in nitrogen. After etching with a hydrofluoric acid solution, the uniform $NiS_x@C$ yolk–shell microboxes are successfully fabricated.

Figure 1b illustrates the phase evolution during the synthetic process. X-ray diffraction (XRD) patterns were used to confirm the crystal structures of the four samples. The precursor can be indexed to NiS_2 (JCPDS No. 01-089-7142), while the $NiS-600$ and $NiS/C-600$ match well with NiS (JCPDS No. 01-077-1624). The $NiS_x@C$ shows a mixed phase of both NiS_2 and NiS. Inductively coupled plasma (ICP) was used to confirm the ratio of NiS and NiS_2 in the composite (Table S1, Supporting Information). Based on the ICP result, the mole ratio of NiS and

NiS_2 is 1: 0.3. It should be mentioned that the SiO_2 layer plays a vital role in this process, apart from generating buffer space. The calcination step in the process serves to carbonize the PFR. However, in parallel to PFR's carbonization, NiS_2 tends to decompose to NiS also at 600 °C (Figure 1b, $NiS-600$), which will drastically reduce the theoretical capacity of the active material due to the decrease in the sulfur content of product.



Surprisingly, after SiO_2 coating, NiS_2 partially remains in the final product even with the same calcination temperature (Figure 1b, $NiS_x@C$). A controlled trial of NiS_2/C without the SiO_2 layer was conducted to reveal the mechanism in this process. The thermogravimetric analysis (TGA) curves of $NiS_2@SiO_2@PFR$ and $NiS_2@PFR$ show that, after SiO_2 coating, the decomposition process of NiS_2 is shifted to higher temperatures (Figure 1c), which leads to the generation of the mixture in the $NiS_x@C$ at 600 °C. The reason for this phenomenon can be explained as follow. The sulfur is in the gaseous state when the temperature is higher than 450 °C. Therefore, for $NiS_2@SiO_2@PFR$, the volatilization of gaseous sulfur was confined by the dense SiO_2 layer, since SiO_2 was stable during the calcination step. As a result, the reaction rate of Equation (1) was greatly decreased which made the decomposition process of NiS_2 shifted to higher temperatures simply due to Le Chatelier's principle.

These results confirm that the silica layer not only provides the buffer space but also maintains the high theoretical capacity of the active material. The weight loss of $NiS_2@SiO_2@PFR$ and $NiS_2@PFR$ both contain two processes: the carbonization of PFR and the decomposition of NiS_2 . Therefore, to determine the decomposition procedure of NiS_2 , the TGA of NiS_2 was also performed in Ar with a heating rate of 5 °C min^{-1} , as shown as Figure S1 in the Supporting Information. Based on the TGA result and previous report,^[27] the decomposition procedure of NiS_2 during calcination can be divided into two steps: 1) $NiS_2 \rightarrow NiS + S$; 2) $3NiS \rightarrow Ni_3S_2 + S$. The TGA curve

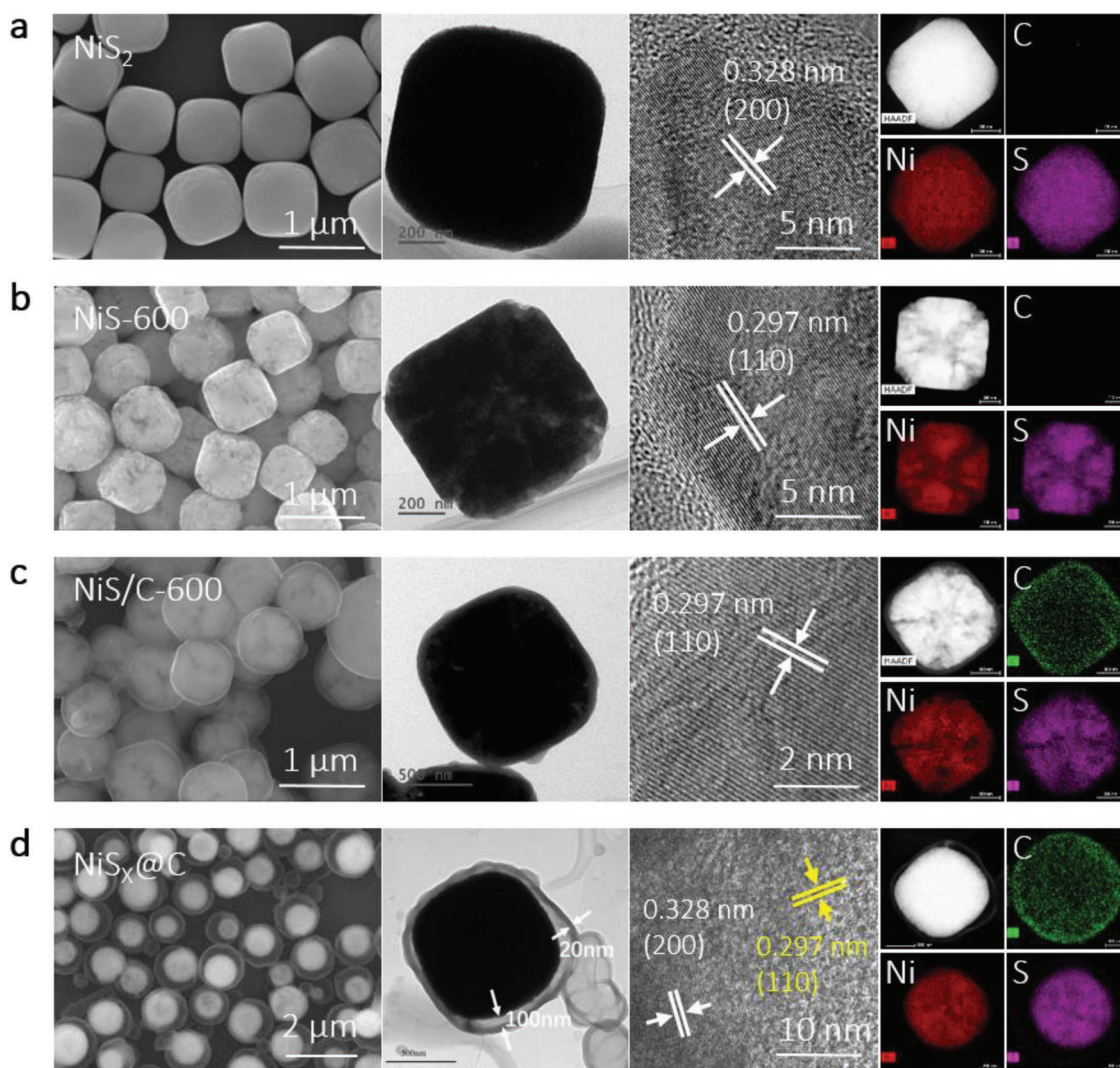


Figure 2. The SEM, TEM, HRTEM images, and EDS elemental mappings of a) NiS_2 , b) NiS-600 , c) NiS/C-600 , and d) $\text{NiS}_x\text{@C}$, respectively.

shows that the weight loss during the decomposition procedure is 26.4% and 9.0%, respectively, which is very close to the theoretical value (26.1% and 8.7%).

Figure 2 displays the morphology and structural characterization of all samples. The field-emission scanning electron microscope (FESEM) and transmission electron microscope (TEM) images clearly show the NiS_2 cubic precursor with an average size of 800 nm and a smooth surface (Figure 2a). After calcination, the NiS-600 still maintains the cubic shape but developed an obvious porous structure, which likely stems from the partial loss of sulfur during the decomposition of NiS_2 (Figure 2b). The NiS/C-600 possesses a core-shell structure with a porous NiS core and a 30 nm carbon shell as confirmed by the TEM and high-angle annular dark field (HAADF) image (Figure 2c and Figure S2c, Supporting Information). There is no gap between the core and shell. Both the SEM and TEM images show distinct yolk-shell $\text{NiS}_x\text{@C}$ microboxes with an obvious void space between the core and shell (Figure 2d and Figure S2d, Supporting Information). Furthermore, the hydrogen fluoride (HF) solution (5 wt%) reacted with NiS_x partly during the etching

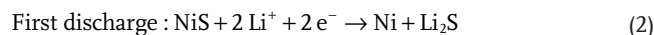
process of silica layer. This reaction is also an etching process and started preferentially from corners due to the high surface energy of corner site, which led to the morphological transformation of cubic NiS_2 to spherical-like NiS_x (Figure 2a,d).^[28] The high-resolution TEM (HRTEM) images in Figure 2 show that the lattice fringes d-spacing of each sample match well with the XRD pattern. Furthermore, TEM-outfitted energy dispersive X-ray spectroscopy (EDS) elemental mapping was applied to confirm the elementary compositions of the samples. All these results suggest that mixed phase NiS_x with a yolk-shell structure ($\text{NiS}_x\text{@C}$) had been constructed successfully.

The XRD patterns show no detected carbon shell diffraction peaks for its amorphous structural feature. Raman spectra were performed to analyze the carbon shell features as shown in Figure S3a in the Supporting Information. Two significant peaks arising at 1350 and 1580 cm^{-1} can be observed for NiS/C-600 and $\text{NiS}_x\text{@C}$, which corresponds to the characteristic D-band (the disordered-induced) and G-band (the graphitic) of carbon, respectively.^[29,30] Furthermore, the carbon content of NiS/C-600 and $\text{NiS}_x\text{@C}$ was verified to be 29.31% and 29.91%, respectively

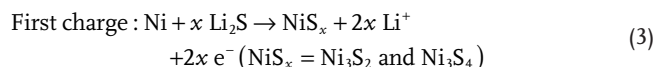
(Table S2, Supporting Information). The pore structure of the as-prepared samples was examined by N₂ adsorption/desorption technique (Figure S3b,c, Supporting Information). The N₂ adsorption/desorption isotherm of the precursor NiS₂ shows no pores with a specific surface area (BET) of 8.67 m² g⁻¹. Both the isotherm of NiS-600 and NiS_x@C can be indexed to the type IV adsorption/desorption isotherm with a clear H4 hysteresis loop, which indicates the narrow slit-like porous structure generated by the decomposition process.^[31] The BET specific surface area is 22.24 and 108.12 m² g⁻¹, respectively. The increased specific area of NiS_x@C is mainly caused by the carbon shell coating. The adsorption pore size distribution (BJH) plot of NiS-600 depicts that its pore sizes mainly concentrate at ≈3.2 nm. On the other hand, the pore sizes of NiS_x@C concentrate at ≈4.2 and ≈24.6 nm, with the additional part coming from the void space generated by the SiO₂ layer.

Most of the metal sulfides possess conversion reactions involving disintegration and reorganization at the molecular level, which results in drastic density changes and ultimately severe pulverization during the discharge/charge process. Therefore, due to the insufficient resolution, general lab XRD is hardly capable of ascertaining the detailed information during conversion reactions. As a result, the Li-storage mechanism of nickel sulfide remains controversial, especially during the first discharge process.^[32,33] Thus, to understand the Li-storage mechanism of NiS_x@C electrodes, we performed in situ synchrotron HEXRD to evaluate the local structural and chemical evolution of the encapsulated active species during the first discharge process (Figure 3). Figure S4a in the Supporting Information shows the discharge/charge curves of NiS_x@C electrode during the first cycle. To eliminate the influence of Cu, the XRD pattern is divided into three parts, 1.8° – 3.0°, 3.25° – 3.5°, and 3.8° – 4.2° (Figure S4b, Supporting Information). During the first discharge, all the peaks of NiS and NiS₂ are gradually weakened without any shift in 2θ from the

beginning (Figure 3). The XRD peaks associated with the Li₂S phase (marked by red arrow) and Ni phase (marked by blue arrow) appear and gradually increase simultaneously (Figure 3). No other phase appears during the discharge process. Since the proportion of NiS₂ is small in the NiS_x@C based on the ICP results (Table S1, Supporting Information), it is difficult to confirm the Li storage mechanism of NiS₂ from the in situ synchrotron HEXRD of the NiS_x@C electrode. On the other hand, NiS is the main component of NiS_x@C. Therefore, the in situ synchrotron HEXRD result demonstrates that the NiS possesses a one-step conversion reaction during the first discharge



Moreover, XRD and TEM were performed to confirm the product of the NiS_x@C electrode after first charge process (Figure S5, Supporting Information). XRD pattern demonstrates that, after first charge, the NiS_x@C electrode consists of Ni₃S₂ and Ni₃S₄, not the original composition (NiS and NiS₂) (Figure S5a, Supporting Information). HRTEM displays the lattice fringes d-spacing of Ni₃S₂ (101) and Ni₃S₄ (311) (Figure S5c, Supporting Information). Therefore, the reaction mechanism of NiS_x@C electrode during first charge process can be deduced as follow



The electrochemical properties for lithium storage was first analyzed by cyclic voltammogram as shown in Figure 4a and Figure S6 in the Supporting Information. It is clearly shown that the initial discharge curves of NiS_x@C, NiS-600, and NiS/C-600 are very different. Compared to NiS-600, carbon coating seems to increase the overpotential during the first discharge process (Figure S6b, Supporting Information). In the following

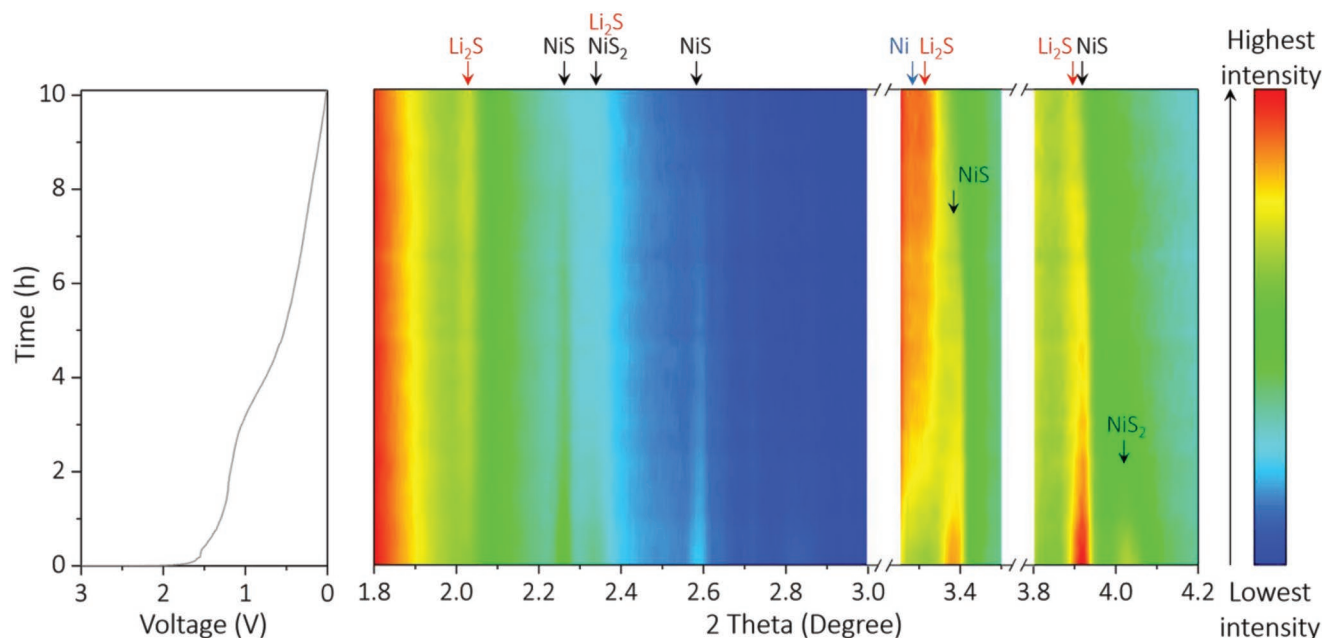


Figure 3. In situ synchrotron HEXRD of NiS_x@C electrode during the first discharge process.

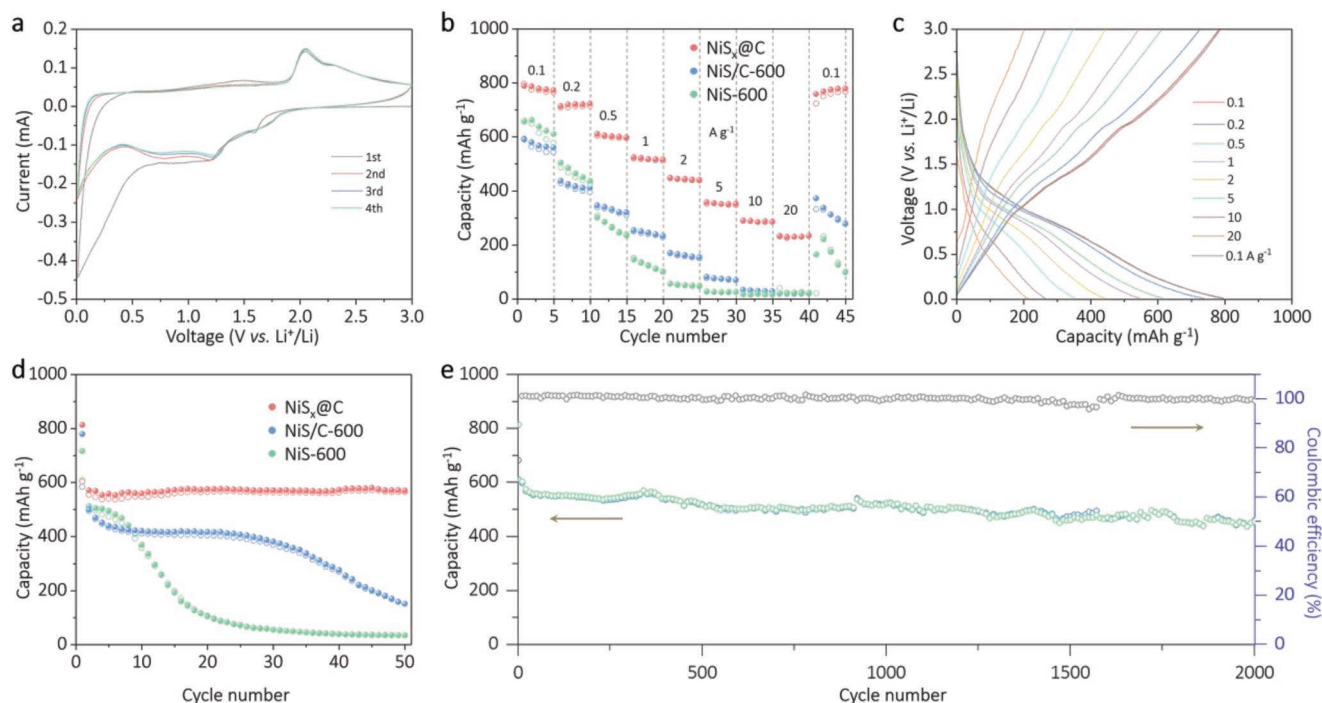


Figure 4. a) Cyclic voltammograms of $\text{NiS}_x\text{@C}$ at a scan rate of 0.1 mV s^{-1} . b) Rate performance of $\text{NiS}_x\text{@C}$, NiS/C-600 , and NiS-600 . c) The corresponding discharge/charge curves of $\text{NiS}_x\text{@C}$ at different current density. d) Cycling performance of $\text{NiS}_x\text{@C}$, NiS/C-600 , and NiS-600 at 1 A g^{-1} . e) Long cycle performance of $\text{NiS}_x\text{@C}$ at 1 A g^{-1} .

cycles, the $\text{NiS}_x\text{@C}$ and NiS/C-600 exhibit similar oxidation and reduction peaks to NiS-600 , but with wider peaks. Figure 4b,c displays the rate performance of these three samples and the corresponding discharge/charge curves of $\text{NiS}_x\text{@C}$. As presented, the $\text{NiS}_x\text{@C}$ electrode displays the best rate performance with average capacities of 790, 720, 605, 540, 446, 350, 280, and 225 mAh g^{-1} at current densities of 0.1, 0.2, 0.5, 1, 2, 5, 10, and 20 A g^{-1} , respectively. When the current density is returned to 0.1 A g^{-1} , the capacity also recovers to 790 mAh g^{-1} , indicating superior reversibility and stability of the constructed $\text{NiS}_x\text{@C}$ yolk-shell structure. The biggest difference between these three samples is the cycling stability. Figure 4d shows the cycling performance of the three as-prepared electrodes at 1 A g^{-1} . The capacity of NiS-600 decays to below 100 mAh g^{-1} in 20 cycles. Benefiting from the carbon coating, the capacity of NiS/C-600 is maintained during the first 20 cycles, but ultimately faded in subsequent cycles. In contrast, $\text{NiS}_x\text{@C}$ exhibits ultrastable cyclability. Even after 2000 cycles at 1 A g^{-1} , the capacity remains at 460 mAh g^{-1} . Meanwhile, the NiS-600 electrode possesses the highest initial Coulombic efficiency of 81.8%. And the initial Coulombic efficiency of $\text{NiS}_x\text{@C}$ and NiS/C-600 electrode is 74.2% and 74.9%, respectively, due to the irreversible capacity of carbon shell in the low-voltage region.^[34] For comparison, $\text{NiS}_x\text{@C}$ structures with different calcination temperatures were also synthesized (Figure S7, Supporting Information). Both $\text{NiS}_x\text{@C-500}$ and NiS@C-700 depict yolk-shell structures and stable cycling performance. However, although $\text{NiS}_x\text{@C-500}$ contains mixed phases that possess high theoretical capacity, the test value is lower than $\text{NiS}_x\text{@C}$ due to poor electrical conductivity resulting from the low calcination temperature. On the other hand, NiS@C-700

also exhibits inferior capacity due to a lower sulfur content arising from the high calcination temperature. It is noteworthy that the thickness of the carbon shell is another crucial factor influencing the electrochemical performance of the electrode. The thickness of carbon layer influences the conductivity and mechanical property of the carbon layer. A thicker carbon layer would reduce the conductivity of the composites and result in an inferior electrochemical performance, especially rate performance, which we have reported previously.^[14] And a $\text{NiS}_x\text{@C}$ composite with thinner carbon layer ($\text{NiS}_x\text{@C-T}$) has also been synthesized, as shown as Figure S8 in the Supporting Information. SEM image shows that, after etching the silica layer, the carbon layer cannot maintain the shell structure and collapse to the NiS_x core due to its poor mechanical property (Figure S8a, Supporting Information). As a result, the $\text{NiS}_x\text{@C-T}$ electrode delivered poor cycling performance, in spite of its high initial capacity (Figure S8b, Supporting Information).

The significant improvement in electrochemical performance of $\text{NiS}_x\text{@C}$ obviously benefits from the construction of the yolk-shell structure. To evaluate the capacity fade mechanism of NiS-600 and the functional mechanism of the carbon coated yolk-shell structure, in situ EIS was performed during the cycling process with a three-electrode system. Figure 5a shows the discharge/charge curve of $\text{NiS}_x\text{@C}$ for the first cycle during the in situ EIS tests. The corresponding in situ time-lapse EIS profiles of $\text{NiS}_x\text{@C}$ during the first discharge and charge process are depicted in Figure 5b,c, respectively. The fitting line (Figure 5d) of a typical Nyquist plot at the full discharge state clearly shows the impedance spectrum, which consists of the resistances of the electrolyte solution (R_s), interfacial layer (R_{surf}), and charge transfer (R_{ct}). Interestingly, the R_{ct} of

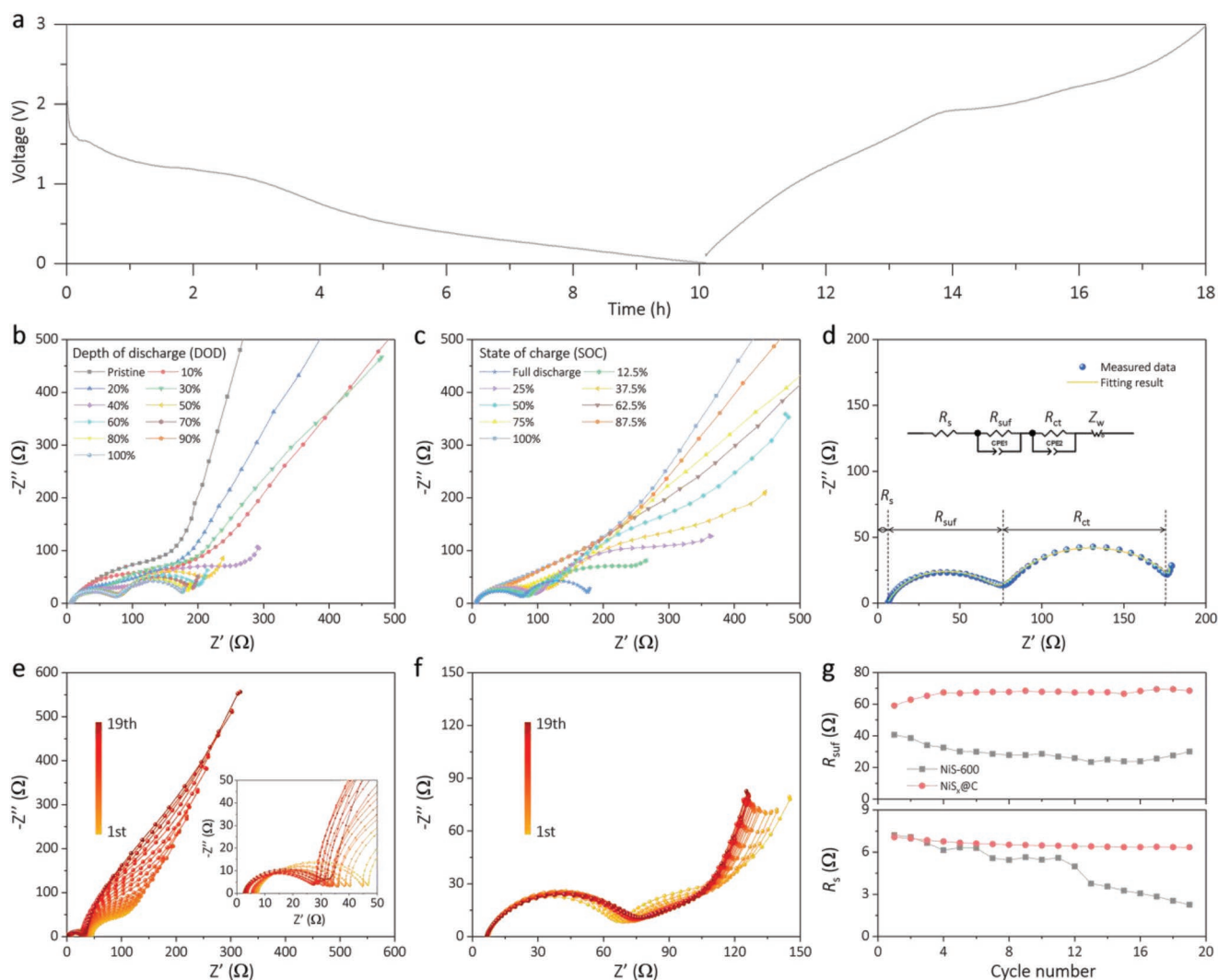


Figure 5. In situ electrochemical impedance spectra characterization of the $\text{NiS}_x\text{@C}$ electrode in comparison with the NiS-600 electrode in three-electrode cells. a) Initial discharge/charge curve of $\text{NiS}_x\text{@C}$ electrode for in situ EIS tests. In situ time-lapse EIS profiles of $\text{NiS}_x\text{@C}$ electrode at b) different depths of discharge (DOD) and c) different states of charge (SOC) during the initial discharge/charge. d) Nyquist plot of a.c. impedance spectra for the $\text{NiS}_x\text{@C}$ electrode measured at full discharge state (inset is the equivalent circuit model). In situ EIS profiles of e) NiS-600 and f) $\text{NiS}_x\text{@C}$ at full discharge state from 1st to 19th cycles. g) Plots of R_s and R_{suf} against cycle number.

$\text{NiS}_x\text{@C}$ gradually emerges and decreases during the discharge process (Figure 5b), followed by an increase and disappearance during the charge process (Figure 5c). NiS-600 also shows a similar trend (Figure S9b,c, Supporting Information). These results indicate that the value of R_{ct} is relevant to the content of Li^+ in the active materials, the more Li^+ the smaller R_{ct} . A plot of R_s and R_{suf} against the state of charge SOC and depth of discharge (DOD) is shown in Figure S9d in the Supporting Information along with the resistances of the NiS-600 for comparison. It is noteworthy that the R_{suf} of $\text{NiS}_x\text{@C}$ at the pristine state is larger than that of NiS-600, which implies that the carbon layer weakens the electronic conductivity of the nickel sulfide. This result indicates that the enhanced rate and cycling performance does not result from the conductivity improvement. Moreover, the R_{suf} of $\text{NiS}_x\text{@C}$ decreases and then increases at the DOD of 40% (≈ 0.8 V vs Li^+/Li), which indicates the formation of the SEI layer. On the contrary, the R_{suf} of

NiS-600 decreases continually during the first discharge process, which may result from the new interface generated by the fracture of particles due to the unlimited volume expansion. This result demonstrates that the carbon layer guarantees the stable formation of the SEI layer and provides a stable environment for the electrochemical reaction.

To further investigate the electrochemical behavior of the electrodes, in situ EIS was collected during the long cycles at 1 A g^{-1} with the three-electrode system. All the EIS profiles were collected at full discharge state (Figure 5e,f and Figure S9e, Supporting Information). The R_s and R_{suf} of the two samples at full discharge state at different cycles are shown in Figure 5g. It is noteworthy that the R_{suf} of $\text{NiS}_x\text{@C}$ increases at the first few cycles and then stabilizes in the following cycles, which implies continuous formation and stabilization of the SEI layer. On the contrary, the R_{suf} of NiS-600 rapidly decreases in the first five cycles and continue to decrease

until the 15th cycle, which indicates severe pulverization of the NiS-600 electrode. Furthermore, TEM image of the NiS-600 electrode after 30 cycles at full charge state shows that the NiS-600 particles have been pulverized to very fine particles after 30 cycles (Figure S11a, Supporting Information). Part of the fine particles even detached from the original particle (red arrow in Figure S11a, Supporting Information) which resulted in the loss of active materials and the generation of microcracks and voids in the electrode (yellow arrow in Figure S11b, Supporting Information). Conversely, the yolk-shell structure still trapped the active material efficiently after 30 cycles (Figure S11d, Supporting Information) and then maintained the good integrity of the NiS_x@C electrode (Figure S11e, Supporting Information). More importantly, R_s of the NiS-600 decreases rapidly during the 6th to 15th cycles, which results from severe dissolution of polysulfide (PS) species into the liquid electrolyte.^[35] However, for NiS_x@C, R_s remains stable throughout the entire cycle. EDS analysis of NiS-600 electrode shows that the ratio of S/Ni is ≈ 0.5 after 30 cycles, which confirms the severe dissolution of PS species into the electrolyte (Figure S11c, Supporting Information). On the contrary, the ratio of S/Ni for NiS_x@C electrode is ≈ 1.22 after 30 cycles, which is very close to the initial value (Figure S11f and Table S1, Supporting Information). In addition, R_{ct} of the NiS-600 gradually increases along with the cycling process, which indicates reduction of Li⁺ content in the discharge product at full discharge state during cycling. Moreover, the inclined line in the low-frequency range indicates the Warburg impedance (Z_w), which results from the Li⁺ diffusion in the bulk of the active material.^[36] The lithium diffusion coefficient can be calculated by following equations

$$D = \frac{R^2 T^2}{2A^2 n^4 F^4 C^2 \sigma^2} \quad (4)$$

$$Z_{re} = R_{ct} + R_e + \sigma \omega^{-1/2} \quad (5)$$

where T is the absolute temperature, R is the gas constant, A is the surface area of the electrode, n is the number of electrons transferred during the reaction, F is the Faraday constant, C is the concentration of Li⁺ in the electrode, D is the diffusion coefficient of Li⁺, and σ is the Warburg factor, which is related to Z_{re} . Therefore, the D value is inversely proportional to the σ^2 value if the C value is constant. Due to the high reversibility and same full discharge state of NiS_x@C electrode, the C value of each plot in Figure 5f can be considered as constant. Based on the results, the relationship between Z_{re} and $\omega^{-1/2}$ can be obtained as shown as Figure S12a in the Supporting Information. Figure S12b in the Supporting Information displays the fitting σ value for different cycles. The results demonstrate that the Li⁺ diffusion coefficient of NiS_x@C electrode at full discharge state increases first and then becomes stable gradually during the cycling process. This result can be attributed to the refinement of the active material particles during the discharge/charge process, which decreases the Li⁺ diffusion length in the electrode.

Therefore, in combination with electrochemical properties, the capacity fade process of NiS-600 can be described as follows:

1) 1st–6th cycles: The particles undergo unlimited expansion to

generate cracks with new interface, which decreases the R_{surf} . SEI layer continues to form on the new interface to separate the discharge Li₂S product from Ni. 2) 6th–15th cycles: The isolated Li₂S convert to PS species during the charge process to dissolve in the liquid electrolyte, which leads to the loss of active material and capacity fade.

Ex situ SEM was performed to illustrate structural changes after the cycle process. Figure 6a clearly shows the crack of NiS-600 after 20 cycles, which corresponds with the in situ EIS results. Although the NiS/C-600 capacity is maintained briefly due to the carbon coating, without the void space between the core and shell the carbon layer will break because of the volume expansion (Figure 6b). Consequently, NiS/C-600 undergoes similar capacity fade after a few cycles. On the contrary, in NiS_x@C electrode the yolk-shell structure is well maintained after 50 cycles and even after 2000 cycles (Figure 6c and Figure S13, Supporting Information). Moreover, TEM of NiS_x@C electrode at full discharge state of different cycles were performed (Figure S14, Supporting Information). Figure S14a,b in the Supporting Information shows that, even at full discharge state, the carbon layer still traps the active material efficiently. Figure S14a in the Supporting Information displays that the thickness of the carbon layer increased to ≈ 180 nm after three cycles due to the formation of SEI layer and the irreversible capacity of carbon shell. After 30 cycles, there is almost no change in the thickness of the carbon layer, both at full discharge and full charge state (Figures S14b and S11d, Supporting Information). This result confirms that the SEI layer is very stable due to the support of the carbon layer. Thus, the significantly improved cycle performance can be mainly attributed to the carbon coated yolk-shell structure, which promotes the formation of a stable SEI layer and offers sufficient space for core expansion that traps active material.

In summary, confined NiS_x@C yolk-shell microboxes have been successfully synthesized through a step-divided construction method for the first time. When applied in Li-ion batteries, the NiS_x@C electrode achieved impressive electrochemical performance, with good long-term cycle life (460 mAh g⁻¹ after 2000 cycles at 1 A g⁻¹), and superior rate performance (225 mAh g⁻¹ at 20 A g⁻¹). The one-step conversion Li-storage mechanism has been demonstrated via in situ synchrotron HEXRD. Moreover, three electrode in situ EIS reveals that the steady SEI layer and stable electrochemical reaction environment are the key factors in improving the performance of conversion type metal sulfide anodes. In addition, this confined yolk-shell structure may introduce new strategies for preparing other transition metal sulfide yolk-shell composites with high reversible capacity and long-term cycle life for high performance electrochemical storage devices.

Experimental Section

Synthesis of Precursor NiS₂ Cubes: NiS₂ cubes were synthesized with a facile solvothermal method. 2 mmol NiCl₂·6H₂O and 4 mmol sulfur powder were dissolved in 60 mL of ethylene glycol in sequence and then stirred for 30 min. Afterward, 0.96 g of polyvinyl pyrrolidone (PVP-K30) was added, followed another 30 min of stirring. The uniform suspension was then transferred to a 100 mL stainless steel autoclave lined with Teflon. After being maintained at 200 °C for 12 h, the precursor NiS₂

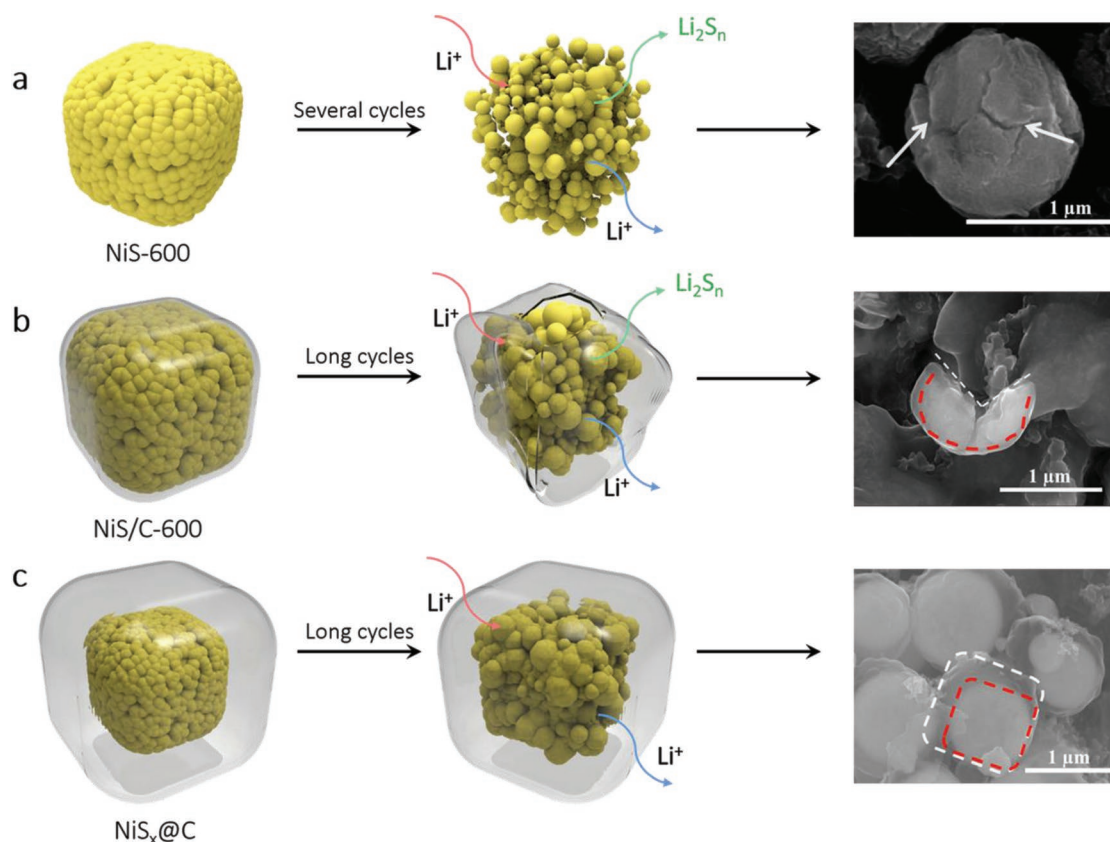


Figure 6. The illustration of structure changes and ex situ SEM of a) NiS-600, b) NiS/C-600, and c) NiS_x@C during cycling process.

cubes were obtained following several washes with ethanol and water and vacuum drying at 60 °C overnight.

Synthesis of NiS_x@C Yolk-Shell Microboxes: 100 mg of the obtained precursor NiS₂ cubes were dispersed in a combined solution of 70 mL ethyl alcohol and 10 mL deionized water. After continuously stirring for 30 min in an ice bath, 3 mL NH₄OH solution and 400 μL tetraethyl orthosilicate (TEOS) solution were added in sequence and the solution was stirred for another 2 h to form the silica layer. Then, 150 mg of resorcinol was added and the solution stirred for 5 min, followed by adding 210 μL of formalin and another 24 h of stirring to finish the condensation reaction. The obtained NiS₂@SiO₂@PFR microcubes were collected and washed several times with ethanol and water. The NiS₂@SiO₂@C was synthesized by annealing the NiS₂@SiO₂@PFR microcubes at 600 °C for 4 h in nitrogen. Finally, the inner silica layer was etched away with HF solution (5 wt%) for one day. Then, the uniform yolk-shell microboxes were obtained, denoted as NiS_x@C. The NiS-600 microcubes were fabricated by directly annealing the NiS₂ at 600 °C for 4 h in nitrogen. The NiS/C-600 microcubes were prepared without the addition of TEOS. NiS_x@C-500 and NiS@C-700 yolk-shell microboxes were prepared by the same procedures as the NiS_x@C, while adjusting the annealing temperature to 500 and 700 °C, respectively. NiS_x@C with thinner carbon layer, denoted as NiS_x@C-T, was also prepared by the same procedures as the NiS_x@C, while adjusting the resorcinol and formalin to 75 mg and 105 μL, respectively.

Structural Characterization: The XRD patterns were collected by a D8 Advance X-ray diffractometer with an area detector, using Cu K_α radiation (λ = 1.5418 Å). FESEM images were collected by JEOL-7100F microscope (with an accelerating voltage of 20 kV). The TEM and HRTEM, HAADF images, and TEM-outfitted EDS elemental mappings analyses were observed by JSM-2010 microscope. Raman spectra were collected by a Renishaw INVIA micro-Raman spectroscopy system and the BET surface areas were measured using a Tristar II 3020 instrument

with adsorption of nitrogen at 77 K. TGA was performed using a Netzsch STA 449 F5 simultaneous analyzer and the samples were heated from room temperature to 1200 °C in Ar with a heating rate of 5 °C min⁻¹.

Electrochemical Characterization: The electrochemical properties were collected in CR2016-type coin half cells with Li metal foil as anode and assembled in an argon-filled glove box. The working electrodes were composed of 80% active material, 15% acetylene black, and 5% carboxyl methyl cellulose binder in weight ratio. The slurry was cast onto Cu foil and dried at 60 °C for 12 h in vacuum. Typically, the mass loading of active materials was around 1.0 mg cm⁻². A solution of 1 M of LiPF₆ in ethylene carbonate (EC) and dimethyl carbonate (DMC) (EC:DMC with 1:1, vol%) was used as electrolyte for LIBs. Galvanostatic charge/discharge measurements were performed using a multichannel battery testing system (LAND CT2001A). Cycling voltammetry was collected with an Autolab potentiostat/galvanostat at original open circuit potential at room temperature.

In Situ EIS Measurements: In situ EIS experiment was performed on a Solartron Analytical 1400 System, using a three electrode cell (purchased from EL-Cell GmbH) with metal lithium as counter and reference electrodes. The cell was assembled and aged in an argon-filled glove box until the open-circuit voltage stabilized. The first discharge/charge test for NiS_x@C and NiS-600 electrode were carried out at 100 mA g⁻¹ between 0.01 and 3.0 V. After every 1 h charge or discharge, the cells stable for 30 min before performing the a.c. impedance were held. For the long cycle in situ EIS, the discharge/charge test was carried out at 1 A g⁻¹ between 0.01 and 3.0 V. After every discharge to 0.01 V, the cells were held stable for 30 min before performing the a.c. impedance. The a.c. amplitude was set at ± 10 mV, the applied frequency range was between 100 kHz and 0.05 Hz.

In Situ Synchrotron Measurements: In situ synchrotron HEXRD measurements during the first cycle were carried out at the 11-ID-C beamline of the Advanced Photon Source, Argonne National Laboratory.

The X-ray beam size was 0.2 mm × 0.2 mm, and the X-ray wavelength was 0.11725 Å. Homemade coin cells were cycled at 100 mA g⁻¹ between 0.01 and 3.0 V using a MACCOR cyclor. During the cell cycling, the XRD patterns were collected every 600 s, using a Perkin-Elmer 2D X-ray detector. The 2D diffraction patterns were then converted into 1D patterns of 2θ versus intensity using GSAS-II software calibrated against a CeO₂ standard.

Supporting Information

Supporting Information is available from the Wiley Online Library or from the author.

Acknowledgements

Q.D.L. and L.L. contributed equally to this work. This work was supported by the National Natural Science Fund for Distinguished Young Scholars (51425204), the National Natural Science Foundation of China (51832004 and 51602239), the National Key R&D Program of China (2016YFA0202601), and the International Science and Technology Cooperation Program of China (2013DFA50840). This work is supported by the U. S. Department of Energy (DOE), Office of Energy Efficiency and Renewable Energy, Vehicle Technologies Office. The support provided for Q.D.L. by the China Scholarship Council (CSC) during a visit to Argonne National Laboratory is also acknowledged. Argonne National Laboratory is operated for DOE Office of Science by UChicago Argonne, LLC, under Contract No. DE-AC02-06CH11357.

Conflict of Interest

The authors declare no conflict of interest.

Keywords

in situ EIS, in situ synchrotron HEXRD, Li-ion battery, long-term cycling stability, nickel sulfide

Received: April 8, 2019
Revised: September 3, 2019
Published online:

- [1] B. Kang, G. Ceder, *Nature* **2009**, 458, 190.
- [2] S. Ovshinsky, M. Fetcenko, J. Ross, *Science* **1993**, 260, 176.
- [3] M. S. Whittingham, *Chem. Rev.* **2004**, 104, 4271.
- [4] S. Chu, Y. Cui, N. Liu, *Nat. Mater.* **2017**, 16, 16.
- [5] D. P. Tabor, L. M. Roch, S. K. Saikin, C. Kreisbeck, D. Sheberla, J. H. Montoya, S. Dwaraknath, M. Aykol, C. Ortiz, H. Tribukait, *Nat. Rev. Mater.* **2018**, 3, 5.
- [6] C.-M. Park, J.-H. Kim, H. Kim, H.-J. Sohn, *Chem. Soc. Rev.* **2010**, 39, 3115.
- [7] J. Zhao, G. Zhou, K. Yan, J. Xie, Y. Li, L. Liao, Y. Jin, K. Liu, P.-C. Hsu, J. Wang, *Nat. Nanotechnol.* **2017**, 12, 993.
- [8] R. Wang, J. Lang, P. Zhang, Z. Lin, X. Yan, *Adv. Funct. Mater.* **2015**, 25, 2270.
- [9] N. Liu, H. Wu, M. T. McDowell, Y. Yao, C. Wang, Y. Cui, *Nano Lett.* **2012**, 12, 3315.
- [10] J. Yang, Y. Wang, W. Li, L. Wang, Y. Fan, W. Jiang, W. Luo, Y. Wang, B. Kong, C. Selomulya, *Adv. Mater.* **2017**, 29, 1700523.
- [11] J. Sun, C. Lv, F. Lv, S. Chen, D. Li, Z. Guo, W. Han, D. Yang, S. Guo, *ACS Nano* **2017**, 11, 6186.
- [12] X. Y. Yu, L. Yu, L. Shen, X. Song, H. Chen, X. W. Lou, *Adv. Funct. Mater.* **2014**, 24, 7440.
- [13] Z. Liu, X.-Y. Yu, X. W. D. Lou, U. Paik, *Energy Environ. Sci.* **2016**, 9, 2314.
- [14] Q. Li, L. Li, K. A. Owusu, W. Luo, Q. An, Q. Wei, Q. Zhang, L. Mai, *Nano Energy* **2017**, 41, 109.
- [15] Q. Li, Q. Wei, Q. An, L. Huang, W. Luo, X. Ren, K. A. Owusu, F. Dong, L. Li, P. Zhou, *Energy Storage Mater.* **2019**, 16, 625.
- [16] S. Suga, A. Kimura, T. Matsushita, A. Sekiyama, S. Imada, K. Mamiya, A. Fujimori, H. Takahashi, N. Mori, *Phys. Rev. B* **1999**, 60, 5049.
- [17] S.-L. Yang, H.-B. Yao, M.-R. Gao, S.-H. Yu, *CrystEngComm* **2009**, 11, 1383.
- [18] S. Friedemann, H. Chang, M. Gamza, P. Reiss, X. Chen, P. Alireza, W. Coniglio, D. Graf, S. Tozer, F. M. Grosche, *Sci. Rep.* **2016**, 6, 25335.
- [19] M. Liu, Y. Chen, J. Su, J. Shi, X. Wang, L. Guo, *Nat. Energy* **2016**, 1, 16151.
- [20] Y. Zhang, F. Lu, L. Pan, Y. Xu, Y. Yang, Y. Bando, D. Golberg, J. Yao, X. Wang, *J. Mater. Chem. A* **2018**, 6, 11978.
- [21] H. Fan, H. Yu, X. Wu, Y. Zhang, Z. Luo, H. Wang, Y. Guo, S. Madhavi, Q. Yan, *ACS Appl. Mater. Interfaces* **2016**, 8, 25261.
- [22] H.-C. Tao, X.-L. Yang, L.-L. Zhang, S.-B. Ni, *J. Electroanal. Chem.* **2015**, 739, 36.
- [23] D. Han, N. Xiao, B. Liu, G. Song, J. Ding, *Mater. Lett.* **2017**, 196, 119.
- [24] X. Li, Y. Chen, J. Zou, X. Zeng, L. Zhou, H. Huang, *J. Power Sources* **2016**, 331, 360.
- [25] Y. Tan, M. Liang, P. Lou, Z. Cui, X. Guo, W. Sun, X. Yu, *ACS Appl. Mater. Interfaces* **2016**, 8, 14488.
- [26] Q. Pan, J. Xie, S. Liu, G. Cao, T. Zhu, X. Zhao, *RSC Adv.* **2013**, 3, 3899.
- [27] H. Kiuchi, K. Funaki, T. Tanaka, *Metall. Trans. B* **1983**, 14, 347.
- [28] H. Shan, W. Gao, Y. Xiong, F. Shi, Y. Yan, Y. Ma, W. Shang, P. Tao, C. Song, T. Deng, *Nat. Commun.* **2018**, 9, 1011.
- [29] Q. Li, Q. Wei, J. Sheng, M. Yan, L. Zhou, W. Luo, R. Sun, L. Mai, *Adv. Sci.* **2015**, 2, 1500284.
- [30] Y. J. Hong, Y. C. Kang, *Small* **2015**, 11, 2157.
- [31] K. S. Sing, *Pure Appl. Chem.* **1985**, 57, 603.
- [32] S.-C. Han, K.-W. Kim, H.-J. Ahn, J.-H. Ahn, J.-Y. Lee, *J. Alloys Compd.* **2003**, 361, 247.
- [33] Y. Wang, Q. Zhu, L. Tao, X. Su, *J. Mater. Chem.* **2011**, 21, 9248.
- [34] E. Buiel, J. R. Dahn, *Electrochim. Acta* **1999**, 45, 121.
- [35] G. Tan, R. Xu, Z. Xing, Y. Yuan, J. Lu, J. Wen, C. Liu, L. Ma, C. Zhan, Q. Liu, *Nat. Energy* **2017**, 2, 17090.
- [36] S. Yi, J. Z. Wang, S. L. Chou, D. Wexler, Y. Wu, *Nano Lett.* **2013**, 13, 1638.